



HAL
open science

Numerical simulations of the Tayler–Spruit dynamo in proto-magnetars

Paul Barrère, Jérôme Guilet, Raphaël Raynaud, Alexis Reboul-Salze

► **To cite this version:**

Paul Barrère, Jérôme Guilet, Raphaël Raynaud, Alexis Reboul-Salze. Numerical simulations of the Tayler–Spruit dynamo in proto-magnetars. *Monthly Notices of the Royal Astronomical Society: Letters*, 2023, 526 (1), pp.L88-L93. 10.1093/mnrasl/slad120 . cea-04232842

HAL Id: cea-04232842

<https://cea.hal.science/cea-04232842>

Submitted on 3 Jan 2024

HAL is a multi-disciplinary open access archive for the deposit and dissemination of scientific research documents, whether they are published or not. The documents may come from teaching and research institutions in France or abroad, or from public or private research centers.

L'archive ouverte pluridisciplinaire **HAL**, est destinée au dépôt et à la diffusion de documents scientifiques de niveau recherche, publiés ou non, émanant des établissements d'enseignement et de recherche français ou étrangers, des laboratoires publics ou privés.



Distributed under a Creative Commons Attribution 4.0 International License

Numerical simulations of the Tayler–Spruit dynamo in proto-magnetars

Paul Barrère¹, Jérôme Guilet¹, Raphaël Raynaud² and Alexis Reboul-Salze³

¹ *Université Paris-Saclay, Université Paris Cité, CEA, CNRS, AIM, F-91191 Gif-sur-Yvette, France*

² *Université Paris Cité, Université Paris-Saclay, CNRS, CEA, AIM, F-91191 Gif-sur-Yvette, France*

³ *Max Planck Institute for Gravitational Physics (Albert Einstein Institute), D-14476 Potsdam, Germany*

Accepted 2023 August 24. Received 2023 August 3; in original form 2023 June 20

ABSTRACT

The Tayler–Spruit dynamo is one of the most promising mechanisms proposed to explain angular momentum transport during stellar evolution. Its development in proto-neutron stars spun-up by supernova fallback has also been put forward as a scenario to explain the formation of very magnetized neutron stars called magnetars. Using three-dimensional direct numerical simulations, we model the proto-neutron star interior as a stably stratified spherical Couette flow with the outer sphere that rotates faster than the inner one. We report the existence of two subcritical dynamo branches driven by the Tayler instability. They differ by their equatorial symmetry (dipolar or hemispherical) and the magnetic field scaling, which is in agreement with different theoretical predictions (by Fuller and Spruit, respectively). The magnetic dipole of the dipolar branch is found to reach intensities compatible with observational constraints on magnetars.

Key words: instabilities – magnetic fields – MHD – stars: magnetars – supernovae: general.

1 INTRODUCTION

Magnetars are a class of neutron stars that exhibit magnetic fields whose dipolar component reaches 10^{14} – 10^{15} G, which makes them the strongest fields observed in the Universe. Their dissipation are thought to power a wide variety of emissions like giant flares (Evans et al. 1980; Hurlley et al. 1999, 2005; Svinin et al. 2021), fast radio bursts (Bochenek et al. 2020; CHIME/FRB Collaboration 2020), and short chaotic X-ray bursts (Gotz et al. 2006; Coti Zelati et al. 2018, 2021). Combined with a millisecond rotation, they may produce magnetorotational explosions, which are more energetic than standard supernovae explosions (Burrows et al. 2007; Dessart et al. 2008; Takiwaki, Kotake & Sato 2009; Bugli et al. 2020, 2023; Kuroda et al. 2020; Obergaulinger & Aloy 2020, 2021, 2022; Bugli, Guilet & Obergaulinger 2021). The origin of these magnetic fields is therefore a crucial question to understand magnetars and their association to extreme events such as gamma-ray bursts or fast radio bursts. Two classes of scenarios can be distinguished for magnetar formation: (i) the merger of a neutron star binary, which may explain the plateau phase and the extended emission in X-ray sources associated with short gamma-ray bursts (Metzger, Quataert & Thompson 2008; Gompertz, O’Brien & Wynn 2014; Lü & Zhang 2014). These events are interesting for their multimessenger signature but are expected to be too rare to be the main formation channel of Galactic magnetars, (ii) the core-collapse of a massive star, which is confirmed by the observation of Galactic magnetars associated with supernova remnants (Vink & Kuiper 2006; Martin et al. 2014; Zhou et al. 2019). In the latter case, the amplification of the magnetic field may be due either to the magnetic flux conservation during the collapse

of the iron core of the progenitor star (Ferrario & Wickramasinghe 2006; Hu & Lou 2009; Schneider et al. 2020) or to a dynamo action in the newly born proto-magnetar. Indeed, two dynamo mechanisms have already been studied by numerical simulations: the convective dynamo (Thompson & Duncan 1993; Raynaud et al. 2020; Masada, Takiwaki & Kotake 2022; Raynaud, Cerdá-Durán & Guilet 2022; White et al. 2022) and the magnetorotational instability (MRI)-driven dynamo (Obergaulinger et al. 2009; Mösta et al. 2014; Reboul-Salze et al. 2021; Guilet et al. 2022; Reboul-Salze et al. 2022). They have been shown to produce magnetar-like magnetic fields for millisecond rotation periods of the proto-magnetar, especially for periods $P \lesssim 10$ ms for the convective dynamo (Raynaud et al. 2020; Raynaud et al. 2022). These scenarios rely on the hypothesis that the rotation of the proto-magnetar is determined by the rotation of the progenitor core. However, it is still uncertain whether there are enough fast-rotating progenitor cores to form all the observed magnetars in the Milky Way, which represent ~ 10 – 40 per cent of the Galactic neutron star population (Kouveliotou et al. 1994; Woods & Thompson 2006; Gill & Heyl 2007; Beniamini et al. 2019).

In Barrère et al. (2022), we developed a new magnetar formation scenario in which the rapid rotation rate of the proto-magnetar is not determined by the progenitor core but by the ejected matter that remains gravitationally bound to the proto-magnetar and eventually falls back on the proto-magnetar surface ~ 5 – 10 s after the core-collapse. Since the accretion is asymmetric, the fallback matter transfers a significant amount of angular momentum to the surface (Chan, Müller & Heger 2020; Janka, Wongwathanarat & Kramer 2022), which makes the surface rotate faster than the core. In Barrère et al. (2022), we argue that this spin-up triggers the amplification of the magnetic field through the Tayler–Spruit dynamo mechanism. This dynamo mechanism can be described as a loop: (i) a poloidal magnetic field is sheared into a toroidal one (Ω -effect), (ii) the toroidal field becomes Tayler unstable after reaching a critical value

* E-mail: paul.barrere@cea.fr (PB); jerome.guilet@cea.fr (JG); raphael.raynaud@cea.fr (RR); alexis.reboul-salze@aei.mpg.de (AR-S)

(Tayler 1973; Pitts & Tayler 1985), and (iii) the Tayler instability regenerates a poloidal field (Fuller, Piro & Jermyn 2019; Skoutnev, Squire & Bhattacharjee 2022; Ji, Fuller & Lecoanet 2023).

The Tayler–Spruit dynamo was first modelled by Spruit (2002) to explain the angular momentum transport in stellar radiative zones. Fuller et al. (2019) provided a revised description, which tackles the previous critics of Spruit’s model (see Denissenkov & Pinsonneault 2007; Zahn, Brun & Mathis 2007). A main difference between both descriptions resides in the saturation mechanism of the dynamo. Spruit (2002) supposes that magnetic energy in the large-scale magnetic field is damped via a turbulent cascade at a rate equal to the growth rate of the Tayler instability, whereas Fuller et al. (2019) rather expect the magnetic energy to cascade from the scale of the instability (and not the large-scale magnetic field) to small scales. This yields distinct magnetic energy damping rates and so different scalings for the saturated magnetic field. Their analytical results are now often included in stellar evolution codes (see e.g. Eggenberger, Maeder & Meynet 2005; Cantiello et al. 2014; Eggenberger, Buldgen & Salmon 2019a; Eggenberger et al. 2019b; Bonanno, Guerrero & Del Sordo 2020; den Hartogh, Eggenberger & Deheuvels 2020; Griffiths et al. 2022). Though this dynamo has long been debated in direct numerical simulations (Braithwaite 2006; Zahn et al. 2007), Petitdemange, Marcotte & Gissinger (2023) recently reported a dynamo solution sharing many characteristics with the Tayler–Spruit model. Their numerical simulations modelled a stellar radiative zone, where the shear is negative, that is, the rotation rate decreases in the radial direction. In this Letter, we demonstrate that the Tayler instability can sustain different dynamo branches in the presence of positive shear, which gives strong support to the magnetar formation scenario of Barrère et al. (2022).

2 NUMERICAL SETUP

We perform three-dimensional (3D) direct numerical simulations of a stably stratified and electrically conducting Boussinesq fluid with the pseudo-spectral code MAGIC (Wicht 2002; Gastine & Wicht 2012; Schaeffer 2013). The fluid has a constant density $\rho = 3.8 \times 10^{14} \text{ g cm}^{-3}$ (which corresponds to a proto-neutron star mass of $M = 1.4 M_{\odot}$) and evolves between two concentric spheres of radius $r_i = 3 \text{ km}$ and $r_o = 12 \text{ km}$, rotating at the angular frequencies Ω_i and $\Omega_o = 2\pi \times 100 \text{ rad s}^{-1}$, respectively. The imposed differential rotation is characterized by the Rossby number $Ro \equiv 1 - \Omega_i/\Omega_o > 0$, which is varied between 0.125 and 1.2. This spherical Taylor–Couette configuration with positive shear prevents the development of the MRI and allows us to study the system in a statistically steady state. We impose no-slip and insulating boundary conditions at the inner and outer spheres. In all the simulations, we keep fixed the other dimensionless control parameters: the shell aspect ratio $\chi \equiv r_i/r_o = 0.25$, the thermal and magnetic Prandtl numbers $Pr \equiv \nu/\kappa = 0.1$ and $Pm \equiv \nu/\eta = 1$, respectively, the Ekman number $E \equiv \nu/(d^2\Omega_o) = 10^{-5}$, and the ratio of the Brunt–Väisälä to the outer angular frequency $N/\Omega_o = 0.1$. The coefficients ν , κ , η , and $d \equiv r_o - r_i$ are respectively the kinematic viscosity, the thermal diffusivity, the resistivity, and the shell width. As discussed in section 1.3 in the Supplemental Materials, the values of the dimensionless parameters are chosen for numerical convenience because realistic parameters of proto-neutron star interiors are out of reach with the current computing power. The magnetic energy is measured by the Elsasser number $\Lambda \equiv B_{\text{rms}}^2/(4\pi\rho\eta\Omega_o)$. The simulations are initialized either from a nearby saturated state, or with a weak ($\Lambda = 10^{-4}$) or a strong ($\Lambda = 10$) toroidal axisymmetric field with a given equatorial symmetry; it

can be either dipolar (i.e. equatorially symmetric¹ with $l = 2, m = 0$) or quadrupolar (i.e. antisymmetric with $l = 1, m = 0$). We define a turbulent resistive time $\bar{\tau}_{\eta} = (\pi r_o/\bar{\ell})^2/\eta \sim 0.2d^2/\eta$, where $\bar{\ell} = 10$ is the typical value of the average harmonic degree of the time-averaged magnetic energy spectrum. In the following, we will term a solution *metastable* when a steady state is sustained for a time interval $\Delta t > 0.3\bar{\tau}_{\eta}$, and *stable* for $\Delta t \geq \bar{\tau}_{\eta}$ (up to $5.7\bar{\tau}_{\eta}$ for the simulation at $Ro = 0.2$).

3 RESULTS

We find in our set of simulations several dynamo branches represented by different colours in the bifurcation diagram shown in Fig. 1. When the differential rotation is low, the flow can not amplify a weak magnetic field (black crosses), but when $Ro > Ro_{\text{W}}^c \sim 0.62$, the magnetic field grows exponentially to reach a metastable or a stable saturated dynamo state (black dots). This kinematic dynamo is driven by an hydrodynamic instability of the Stewartson layer whose threshold is $Ro_{\text{hyd}}^c \sim 0.175$ (dashed vertical black line), which is in agreement with Hollerbach (2003). When $Ro \gtrsim 0.8$, the kinematic growth is followed by a non-linear growth and the system transitions directly to another branch with a larger magnetic energy (green circles). Restarting from a nearby saturated solution or a strong toroidal field with quadrupolar symmetry (mauve dashed arrows), we find that the stability of this branch extends to Rossby number as low as $Ro_{\text{H}}^c \sim 0.37 < Ro_{\text{W}}^c$, which indicates that this dynamo is subcritical. By starting from a strong toroidal field with dipolar symmetry, we observe that this subcritical branch is in bistability with another one which presents even stronger saturated magnetic fields $B_{\text{rms}} \in [4 \times 10^{14}, 1.1 \times 10^{15}] \text{ G}$ (red circles). This branch is also subcritical since it can be maintained for Rossby numbers as low as $Ro > Ro_{\text{D}}^c \sim 0.19$. Moreover, the two subcritical branches do not only differ by their magnetic field strength but also by their equatorial symmetry, as seen in the 3D snapshots and the surface maps of the magnetic field in Fig. 1. Indeed, the magnetic field shows a dipolar symmetry on the stronger dynamo branch, whereas it is hemispherical on the weaker one. The latter can be interpreted as the superposition of modes with opposite equatorial symmetry (Gallet & Pétrelis 2009), which is consistent with the fact that we do find quadrupolar solutions (mauve circles in Fig. 1). These are only metastable for $Ro > Ro_{\text{Q}}^c \sim 0.7$ and transition to a stable dipolar or hemispherical solution. Finally, we note that the hemispherical dynamos with $Ro \gtrsim 0.8$ (light green circles in Figs 1 and 2) display parity modulations (i.e. the solution evolves between hemispherical, dipole, and quadrupole symmetric states). This behaviour is reminiscent of the so-called Type 1 modulation identified in other dynamo set-ups (Knobloch, Tobias & Weiss 1998; Raynaud & Tobias 2016) and likely results from the coupling of modes with opposite parity as the equatorial symmetry breaking of the flow increases at larger Rossby numbers.

The difference between the three dynamo branches is also clear in Fig. 2, where we see that the hemispherical branch saturates below the equipartition, with an energy ratio increasing with Ro from ~ 0.014 up to ~ 0.56 . By contrast, the dynamos of the dipolar branch are in a superequipartition state ($E_b/E_k > 1$) and follow the magnetostrophic scaling $E_b/E_k \propto Ro^{-1}$ characteristic of the Coriolis–Lorenz force balance (Roberts & Soward 1972; Dormy 2016; Aubert, Gastine & Fournier 2017; Dormy, Oruba & Petitdemange 2018; Augustson, Brun & Toomre 2019; Schwaiger, Gastine & Aubert

¹For the choice of these definitions, see Gubbins & Zhang (1993).

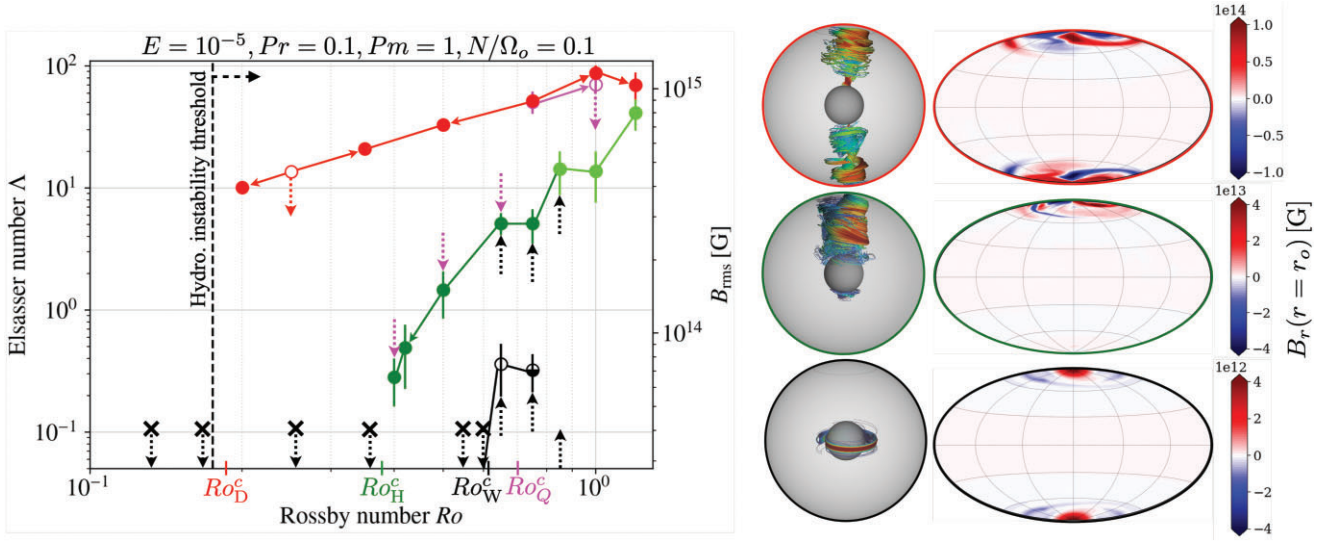


Figure 1. Left: Bifurcation diagram of the time and volume averaged Elsasser number (and root mean square magnetic field) versus the Rossby number. Distinct dynamo branches are represented: dipolar (red), quadrupolar (mauve), hemispherical (green), and kinematic (black) whose respective thresholds are $Ro_D^c \sim 0.19$, $Ro_Q^c \sim 0.7$, $Ro_H^c \sim 0.37$, and $Ro_W^c \sim 0.62$. The hydrodynamic instability is triggered for $Ro_{\text{hyd}} > 0.177$. Dark green circles are stationary hemispherical dynamos and light green ones display parity modulations. Black crosses indicate failed dynamos, empty circles metastable solutions. Arrows attached to circles indicate the initial condition of the associated simulation. The black half empty circle specifies that the solution was found to be metastable in a simulation and stable in another. The error bars indicate the standard deviation. Right: snapshots of the magnetic field lines and surface radial fields associated to the different main dynamo branches at $Ro = 0.75$: dipolar (top), hemispherical (middle), and kinematic (bottom).

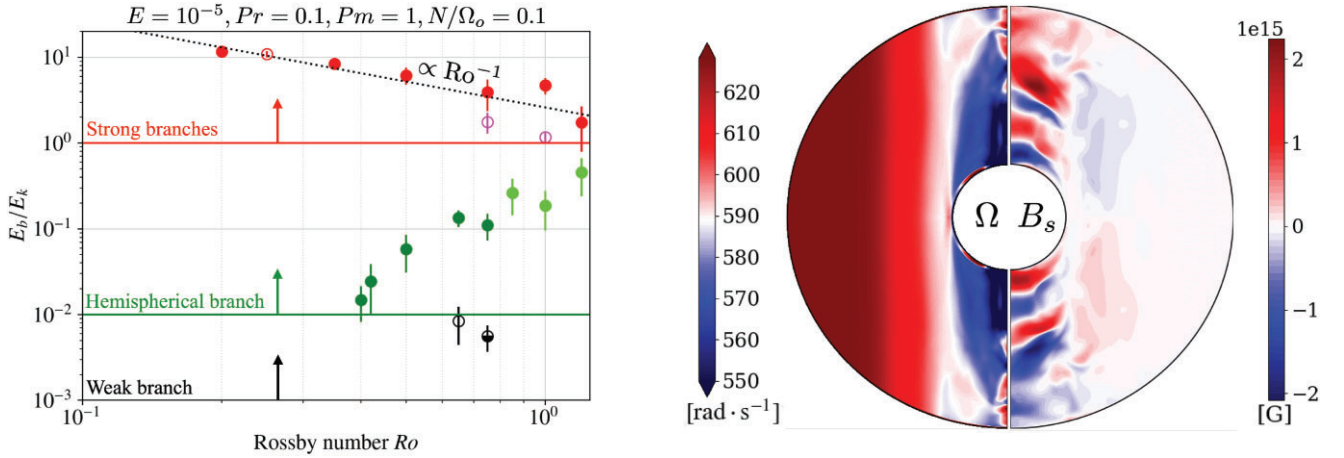


Figure 2. Time-averaged ratio of the magnetic energy to the kinetic energy densities as a function of the Rossby number. The error bars indicate the standard deviation.

2019; Seshasayanan & Gallet 2019; Raynaud et al. 2020). This is also confirmed by force balance spectra shown in fig. S1 in the Supplemental Materials.

Both subcritical dynamos show magnetic fields concentrated along the rotation axis, which differs significantly from the subcritical solutions found with a negative shear by (Petitdemange et al. 2023); this is also strikingly different from the magnetic field generated on the equatorial plane by the kinematic dynamo (see 3D snapshots of Fig. 1). This suggests that the dipolar and hemispherical dynamos are driven by a different mechanism. We argue that they are driven by the Taylor instability according to the following arguments. First, the axisymmetric toroidal magnetic component is clearly dominant since it contains 53–88 per cent of the total magnetic energy. Second, the simulations show a poloidal magnetic field with a dominant $m = 1$

Figure 3. Snapshots of the azimuthal slices of the angular velocity (left) and the magnetic field along the cylindrical radius $s \equiv r \sin \theta$ (right) of the dipolar dynamo at $Ro = 0.75$.

mode (see Supplemental Materials figs S2 and S3), which is the most unstable mode of the Taylor instability (Zahn et al. 2007; Ma & Fuller 2019). In the azimuthal cut of the magnetic field component B_s in Fig. 3, the Taylor mode also appears clearly close to the poles, where it is expected to develop for a toroidal field generated by the shearing of a poloidal field (see Supplemental Materials fig. S4). This is also consistent with the 3D snapshots of the dipolar and hemispherical branches in Fig. 1 where the toroidal magnetic field seems prone to a kink instability. Third, as in Petitdemange et al. (2023), the system bifurcates from the kinematic to the hemispherical branch in the vicinity of the threshold of the Taylor instability (Spruit 1999, 2002)

$$\Lambda_\phi^c \equiv \frac{B_\phi^c{}^2}{4\pi\rho\eta\Omega_o} \sim \frac{\chi}{1-\chi} \frac{N}{\Omega_o} \sqrt{\frac{Pr}{E}} \sim 3.3. \quad (1)$$

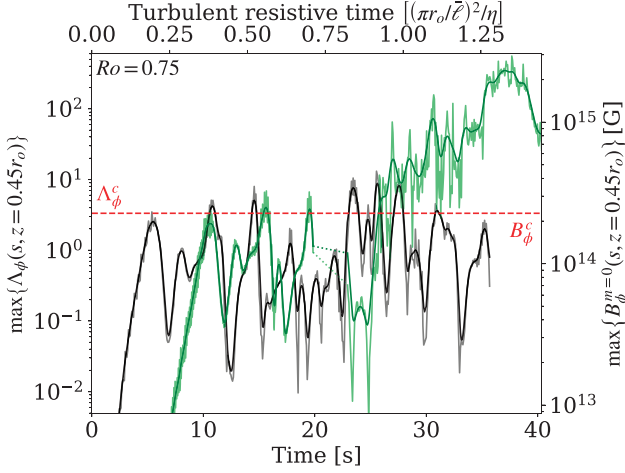


Figure 4. Time series of the maximum along the cylindrical radius s of the axisymmetric toroidal magnetic energy measured locally at $z = 0.45r_o$, for stable (black) and metastable (green) kinematic dynamos at $Ro = 0.75$. The dashed red line indicates the analytical threshold of the Tayler instability (equation 1). Dark lines show a running average and dotted green lines around $t \sim 20$ s indicate missing data.

Indeed, if we focus on the stable and metastable kinematic solutions found at $Ro = 0.75$, we see in Fig. 4 that the *local* maximum of the toroidal axisymmetric field is in both cases close to the critical value above which it is expected to become unstable. The bifurcation from the kinematic toward the hemispherical branch that is observed for the metastable solution appears hence as the result of turbulent fluctuations departing far enough above the threshold of the Tayler instability.

Finally, we compare our numerical results to the theoretical predictions regarding the saturation of the Tayler–Spruit dynamo. Note that these predictions assume the scale separation $\omega_A \ll \Omega_o \ll N$, where the Alfvén frequency is defined by $\omega_A \equiv B_\phi / \sqrt{4\pi\rho r_o^2} \sim 12.1 (B_\phi / 10^{15} \text{ G}) \text{ Hz}$. Our numerical models assume $N/\Omega_o = 0.1$ to limit the computational costs, whereas for a typical PNS spun-up by fallback to a period of 1–10 ms we expect $N/\Omega_o \sim 1$ –10. On the other hand, the achieved magnetic field follows the right scale separation with $\omega_A/\Omega_o \lesssim 0.02$, which is expected to determine the saturation mechanism of the Tayler instability (Ji et al. 2023). Fig. 5 displays the axisymmetric toroidal and poloidal magnetic fields (top), the dipole field (middle) and the Maxwell torque (bottom) as a function of an effective shear rate q measured locally in the saturated state of the dynamo (see Supplemental Materials fig. S5). For the dipolar branch (red), we find that the power laws $B_{\text{tor}}^{m=0} \propto q^{0.36 \pm 0.05}$ and $B_{\text{pol}}^{m=0} \propto q^{0.62 \pm 0.07}$ fit the saturated magnetic field, while we find $B_s B_\phi \propto q^{1.0 \pm 0.02}$ or $B_s^{m=0} B_\phi^{m=0} \propto q^{1.1 \pm 0.04}$, depending on whether we take into account non-axisymmetric contributions to compute the Maxwell torque T_M . The scaling exponents are thus in good agreement with the theoretical predictions of Fuller et al. (2019) $B_{\text{tor}}^{m=0} \propto q^{1/3}$, $B_{\text{pol}}^{m=0} \propto q^{2/3}$, and $T_M \propto q$ (red dotted lines in Fig. 5). Contrary to their prediction, however, our torque is not dominated by the axisymmetric magnetic field, which may be related to their assumption of a stronger stratification. Interestingly, the hemispherical branch (green) does not follow the same scalings: for $q \geq 0.2$, we find $B_{\text{tor}}^{m=0} \propto q^{2.1 \pm 0.31}$ and $B_{\text{pol}}^{m=0} \propto q^{2.0 \pm 0.28}$ for the magnetic field, and $B_s B_\phi \propto q^{2.7 \pm 0.40}$ or $B_s^{m=0} B_\phi^{m=0} \propto q^{3.8 \pm 0.70}$ for the Maxwell torque. These results globally support Spruit’s predictions (Spruit 2002) $B_{\text{tor}}^{m=0} \propto q$, $B_{\text{pol}}^{m=0} \propto q^2$, and $T_M \propto q^3$ (green

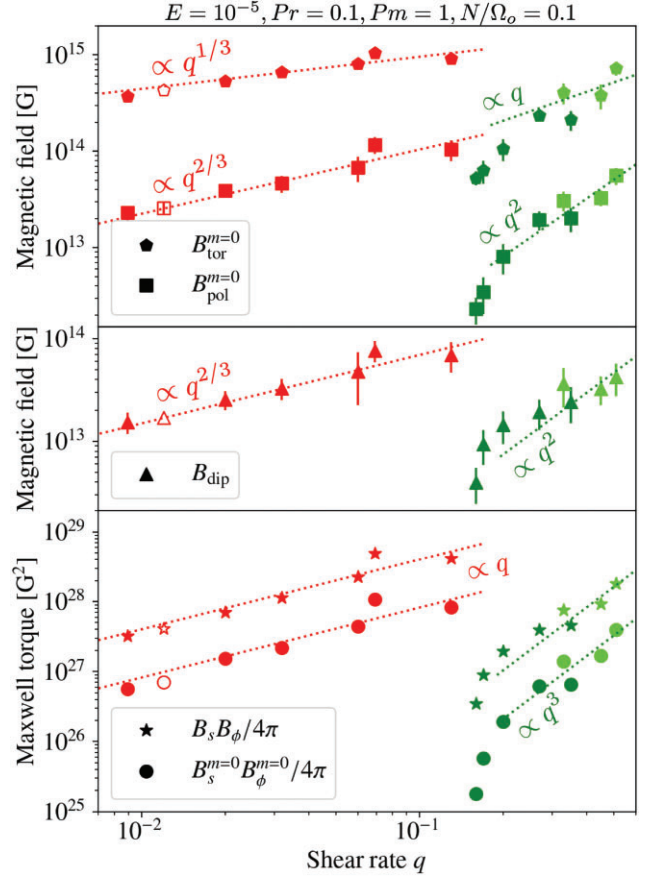


Figure 5. Root mean square (RMS) toroidal and poloidal axisymmetric magnetic fields (top), RMS magnetic dipole (middle), and RMS magnetic torque (bottom) as a function of the time-averaged shear rate measured in the steady state, for the dipolar (red) and hemispherical (green) dynamo branches. Dotted lines show the best fits obtained with Fuller’s (red) and Spruit’s (green) theoretical scaling laws, respectively.

dotted lines)². If we focus on the dipole field, we find the following power laws: $B_{\text{dip}} \propto q^{0.66 \pm 0.03}$ and $B_{\text{dip}} \propto q^{1.1 \pm 0.4}$, for the dipolar and hemispherical branches, respectively. The dipole field on the strong branch therefore follows the same scaling as the axisymmetric poloidal field and is only ~ 33 per cent weaker.

4 CONCLUSIONS

To conclude, we show that the Tayler–Spruit dynamo also exists in the presence of positive shear. We demonstrate for the first time the existence of two subcritical branches of this dynamo with distinct equatorial symmetries, dipolar, and hemispherical. Moreover, the former follows Fuller’s theoretical predictions, while the latter is in overall agreement with Spruit’s model. Compared to the study of Petitdemange et al. (2023) that use a negative shear, our results present a similar dynamical structure, with a bifurcation diagram characterized by a bistability between kinematic and subcritical dynamo solutions. The magnetic field of their Tayler–Spruit dynamo

²In the case of the toroidal magnetic field, the power-law index from the fit is in slight tension with the theoretical prediction. However, this tension is not very significant: it is driven mainly by a single data point and disappears if we change the threshold from $q > 0.2$ to $q > 0.25$ to exclude the model $Ro = 0.5$ as with $q = 0.2$.

is, however, different since it is characterized by a smaller scale structure localized near the inner boundary in the equatorial plane, and induces a torque scaling according to Spruit's prediction. Our study shows a magnetic field geometry concentrated near the pole in agreement with the expectation of the Taylor–Spruit dynamo and a more complex physics, with the existence of two different branches that can not be captured by a single scaling law. Extended parameter studies will be needed to further assess the impact of the resistivity and the stratification on this dynamo instability and better constrain its astrophysical implications.

Our results are of particular importance for stellar evolution models by confirming the existence of the Taylor–Spruit dynamo and by deepening our physical understanding of its complex dynamics. They also give strong support to the new magnetar formation scenario proposed by Barrère et al. (2022), which relies on the development of a Taylor-instability driven dynamo in the presence of a positive shear. We validate the assumption that the magnetic dipole is a significant fraction of the poloidal magnetic field and follows the same scaling. Extrapolating our results for the dipolar branch to $q \sim 1$ as expected in Barrère et al. (2022), we obtain a magnetic dipole intensity of $\sim 3.2 \times 10^{14}$ G and an even stronger axisymmetric toroidal field of $\sim 2.1 \times 10^{15}$ G. These orders of magnitude are similar to those found in Barrère et al. (2022) for the same rotation period of $P_o \equiv 2\pi/\Omega_o = 10$ ms, and fall right in the magnetar range (Olausen & Kaspi 2014).

ACKNOWLEDGEMENTS

We thank F. Daniel, C. Gissinger, and L. Petitdemange and F. Marcotte for fruitful discussions and for sharing the manuscript Petitdemange et al. (2023) before its publication. We also thank A. Igoshev for valuable comments. This work was supported by the European Research Council (MagBURST grant 715368), and the Programme National Physique Stellaire (PNPS) and the Programme National Hautes Énergies (PNHE) programmes of CNRS/INSU, co-funded by CEA and CNES. Numerical simulations have been carried out at the Centre Informatique National de l'Enseignement Supérieur (CINES) on the Jean-Zay supercomputer (DARI project A0130410317).

DATA AVAILABILITY

The data underlying this article will be shared on reasonable request to the corresponding author.

REFERENCES

Aubert J., Gastine T., Fournier A., 2017, *J. Fluid Mech.*, 813, 558
 Augustson K. C., Brun A. S., Toomre J., 2019, *ApJ*, 876, 83
 Barrère P., Guilet J., Reboul-Salze A., Raynaud R., Janka H. T., 2022, *A&A*, 668, A79
 Beniamini P., Hotokezaka K., van der Horst A., Kouveliotou C., 2019, *MNRAS*, 487, 1426
 Bochenek C. D., Ravi V., Belov K. V., Hallinan G., Kocz J., Kulkarni S. R., McKenna D. L., 2020, *Nature*, 587, 59
 Bonanno A., Guerrero G., Del Sordo F., 2020, *Mem. Soc. Astron. Ital.*, 91, 249
 Braithwaite J., 2006, *A&A*, 449, 451
 Bugli M., Guilet J., Obergaulinger M., Cerdá-Durán P., Aloy M. A., 2020, *MNRAS*, 492, 58
 Bugli M., Guilet J., Obergaulinger M., 2021, *MNRAS*, 507, 443
 Bugli M., Guilet J., Foglizzo T., Obergaulinger M., 2023, *MNRAS*, 520, 5622
 Burrows A., Dessart L., Livne E., Ott C. D., Murphy J., 2007, *ApJ*, 664, 416
 CHIME/FRB Collaboration, 2020, *Nature*, 587, 54

Cantiello M., Mankovich C., Bildsten L., Christensen-Dalsgaard J., Paxton B., 2014, *ApJ*, 788, 93
 Chan C., Müller B., Heger A., 2020, *MNRAS*, 495, 3751
 Coti Zelati F., Rea N., Pons J. A., Campana S., Esposito P., 2018, *MNRAS*, 474, 961
 Coti Zelati F. et al., 2021, *ApJ*, 907, L34
 den Hartogh J. W., Eggenberger P., Deheuvels S., 2020, *A&A*, 634, L16
 Denissenkov P. A., Pinsonneault M., 2007, *ApJ*, 655, 1157
 Dessart L., Burrows A., Livne E., Ott C. D., 2008, *ApJ*, 673, L43
 Dormy E., 2016, *J. Fluid Mech.*, 789, 500
 Dormy E., Oruba L., Petitdemange L., 2018, *Fluid Dyn. Res.*, 50, 011415
 Eggenberger P., Maeder A., Meynet G., 2005, *A&A*, 440, L9
 Eggenberger P., Buldgen G., Salmon S. J. A. J., 2019a, *A&A*, 626, L1
 Eggenberger P., den Hartogh J. W., Buldgen G., Meynet G., Salmon S. J. A. J., Deheuvels S., 2019b, *A&A*, 631, L6
 Evans W. D. et al., 1980, *ApJ*, 237, L7
 Ferrario L., Wickramasinghe D., 2006, *MNRAS*, 367, 1323
 Fuller J., Piro A. L., Jermyn A. S., 2019, *MNRAS*, 485, 3661
 Gallet B., Pétrelis F., 2009, *Phys. Rev. E*, 80, 035302
 Gastine T., Wicht J., 2012, *Icarus*, 219, 428
 Gill R., Heyl J., 2007, *MNRAS*, 381, 52
 Gompertz B. P., O'Brien P. T., Wynn G. A., 2014, *MNRAS*, 438, 240
 Gotz D. et al., 2006, *Astron. Telegram*, 953, 1
 Griffiths A., Eggenberger P., Meynet G., Moyano F., Aloy M.-Á., 2022, *A&A*, 665, A147
 Gubbins D., Zhang K., 1993, *Phys. Earth Planet. Inter.*, 75, 225
 Guilet J., Reboul-Salze A., Raynaud R., Bugli M., Gallet B., 2022, *MNRAS*, 516, 4346
 Hollerbach R., 2003, *J. Fluid Mech.*, 492, 289
 Hu R.-Y., Lou Y.-Q., 2009, *MNRAS*, 396, 878
 Hurley K. et al., 1999, *Nature*, 397, 41
 Hurley K. et al., 2005, *Nature*, 434, 1098
 Janka H.-T., Wongwathanarat A., Kramer M., 2022, *ApJ*, 926, 9
 Ji S., Fuller J., Lecoanet D., 2023, *MNRAS*, 521, 5372
 Knobloch E., Tobias S. M., Weiss N. O., 1998, *MNRAS*, 297, 1123
 Kouveliotou C. et al., 1994, *Nature*, 368, 125
 Kuroda T., Arcones A., Takiwaki T., Kotake K., 2020, *ApJ*, 896, 102
 Lü H.-J., Zhang B., 2014, *ApJ*, 785, 74
 Ma L., Fuller J., 2019, *MNRAS*, 488, 4338
 Martin J., Rea N., Torres D. F., Papitto A., 2014, *MNRAS*, 444, 2910
 Masada Y., Takiwaki T., Kotake K., 2022, *ApJ*, 924, 75
 Metzger B. D., Quataert E., Thompson T. A., 2008, *MNRAS*, 385, 1455
 Mösta P. et al., 2014, *ApJ*, 785, L29
 Obergaulinger M., Aloy M. Á., 2020, *MNRAS*, 492, 4613
 Obergaulinger M., Aloy M. Á., 2021, *MNRAS*, 503, 4942
 Obergaulinger M., Aloy M. Á., 2022, *MNRAS*, 512, 2489
 Obergaulinger M., Cerdá-Durán P., Müller E., Aloy M. A., 2009, *A&A*, 498, 241
 Olausen S. A., Kaspi V. M., 2014, *ApJS*, 212, 6
 Petitdemange L., Marcotte F., Gissinger C., 2023, *Science*, 379, 300
 Pitts E., Tayler R. J., 1985, *MNRAS*, 216, 139
 Raynaud R., Tobias S. M., 2016, *J. Fluid Mech.*, 799, R6
 Raynaud R., Guilet J., Janka H.-T., Gastine T., 2020, *Sci. Adv.*, 6, eaay2732
 Raynaud R., Cerdá-Durán P., Guilet J., 2022, *MNRAS*, 509, 3410
 Reboul-Salze A., Guilet J., Raynaud R., Bugli M., 2021, *A&A*, 645, A109
 Reboul-Salze A., Guilet J., Raynaud R., Bugli M., 2022, *A&A*, 667, A94
 Roberts P. H., Soward A. M., 1972, *Annu. Rev. Fluid Mech.*, 4, 117
 Schaeffer N., 2013, *Geochem. Geophys. Geosyst.*, 14, 751
 Schneider F. R. N., Ohlmann S. T., Podsiadlowski P., Röpké F. K., Balbus S. A., Pakmor R., 2020, *MNRAS*, 495, 2796
 Schwaiger T., Gastine T., Aubert J., 2019, *Geophys. J. Int.*, 219, S101
 Seshasayanan K., Gallet B., 2019, *J. Fluid Mech.*, 864, 971
 Skoutnev V., Squire J., Bhattacharjee A., 2022, *MNRAS*, 517, 526
 Spruit H. C., 1999, *A&A*, 349, 189
 Spruit H. C., 2002, *A&A*, 381, 923
 Svinikin D. et al., 2021, *Nature*, 589, 211
 Takiwaki T., Kotake K., Sato K., 2009, *ApJ*, 691, 1360
 Taylor R. J., 1973, *MNRAS*, 161, 365

- Thompson C., Duncan R. C., 1993, *ApJ*, 408, 194
Vink J., Kuiper L., 2006, *MNRAS*, 370, L14
White C. J., Burrows A., Coleman M. S. B., Vartanyan D., 2022, *ApJ*, 926, 111
Wicht J., 2002, *Phys. Earth Planet. Inter.*, 132, 281
Woods P. M., Thompson C., 2006, in Lewin W., van der Klis M., eds, *Compact stellar X-ray sources* Vol. 39. Cambridge Univ. Press, Cambridge, p. 547
Zahn J. P., Brun A. S., Mathis S., 2007, *A&A*, 474, 145
Zhou P., Vink J., Safi-Harb S., Miceli M., 2019, *A&A*, 629, A51

SUPPORTING INFORMATION

Supplementary data are available at *MNRASL* online.

suppl_data

Please note: Oxford University Press is not responsible for the content or functionality of any supporting materials supplied by the authors. Any queries (other than missing material) should be directed to the corresponding author for the article.

This paper has been typeset from a \TeX/L\TeX file prepared by the author.